





# Effect of $ZrB_2$ Particle Size on Pressureless Sintering of $ZrB_2$ - $\beta$ -SiC Composites

Rosa Maria da Rocha<sup>1\*</sup>, Frank Ferrer Sene<sup>1</sup>, Mariah de Oliveira Juliani<sup>2</sup>, Caroline Oliveira Davi<sup>2</sup>

Rocha RM  <https://orcid.org/0000-0002-4090-3496>  
Sene FF  <https://orcid.org/0000-0001-6885-043X>  
Juliani MO  <https://orcid.org/0000-0002-0596-447X>  
Davi CO  <https://orcid.org/0000-0002-7198-7856>

## How to cite

Rocha RM; Sene FF; Juliani MO; Davi CO (2019) Effect of  $ZrB_2$  Particle Size on Pressureless Sintering of  $ZrB_2/\beta$ -SiC Composites. J Aerosp Technol Manag, 11: e2819. <https://doi.org/10.5028/jatm.v11.1049>

**ABSTRACT:** Zirconium diboride is an ultra high temperature ceramic material that leads this emerging class of materials because of its distinct combination of properties, including high melting temperature (> 3000 °C) and the lowest theoretical density (6.09 g·cm<sup>-3</sup>) among the borides. This combination of properties makes  $ZrB_2$  candidate for airframe leading edges on sharp-bodied reentry vehicles. In this work, the effect of particle size of  $ZrB_2$  on the pressureless sintering of  $ZrB_2$ -SiC composites was studied, using  $ZrB_2$  powder with average particle size of 2.6 and 14.2 μm. Four different vol% concentration of  $\beta$ -SiC (0, 10, 20 and 30 vol%) were added to as-received and planetary milled  $ZrB_2$  powder. Samples were pressureless sintered at 2050 °C/1h in argon atmosphere. The reduction of initial  $ZrB_2$  particle size led to composites with better results of densification, mechanical properties and oxidation resistance regardless  $\beta$ -SiC addition, showing relative densities around 92.5 %Theoretical Density (Td) and flexural strength and microhardness around 260 MPa and 17.5 GPa, respectively. Composites processed with as-received  $ZrB_2$  powder showed increasing in densification and flexural strength with the SiC content increasing. Relative density varied from 74.7 to 90.8 %TD and flexural strength from 102 to 241 MPa, for 0 and 30 vol% of SiC, respectively.

**KEYWORDS:** Ultra high temperature ceramics,  $ZrB_2$ , SiC, Sintering, Thermal protection system.

## INTRODUCTION

Reusable atmospheric reentry vehicles and hypersonic flight vehicles, regardless of their specific designs, require control surface with sharp leading edges (radius as low as 1 cm or less) in order to increase the range of hypersonic flight paths and reentry trajectories (Boyd and Padilla 2003; Loehman *et al.* 2006; Szirczak and Smith 2016). However, low-radius edges are subject to much greater aerothermal heating than blunt edges, such as those of the space shuttle. The temperature of the leading edge is inversely proportional to the square root of its radius, in other words, the more aerodynamic the shape, the higher the temperature (Kontinos *et al.* 2001). Flight trajectories having rapid acceleration to Mach 10 impose significant heat fluxes and mechanical stress associated with vibration (Rolim *et al.* 2011; Van Wie *et al.* 2004). For example, the temperatures at a blunt leading edge like the space shuttle orbiter are approximately 1650 °C. For hypersonic vehicles with sharp aerosurfaces (engine cowl inlets, wing leading edges and nosecones), there are foreseeable needs for reusable materials that can withstand temperatures of 2000 °C or above operating in air (Opeka *et al.* 2004; Squire and Marschall 2010; Walker and Sullivan 2003).

Currently, structural materials for use in high temperature oxidizing environments are limited to SiC or  $Si_3N_4$  based composites, oxide ceramics and carbon fiber composites with thermal protection. SiC based ceramics and protected C/C composites exhibit

1. Departamento de Ciência e Tecnologia Aeroespacial – Instituto de Aeronáutica e Espaço – Divisão de Materiais – São José dos Campos/SP – Brazil.

2. Universidade de São Paulo – Escola de Engenharia de Lorena – Lorena/SP – Brazil.

\*Correspondence author: [rosa.rocha11@gmail.com](mailto:rosa.rocha11@gmail.com)

Received: Mar. 6, 2018 | Accepted: Oct. 4, 2018

Section Editor: Mariana Fraga



good oxidation resistance only up to  $\sim 1600$  °C, and their thermal cycling lifetimes are modest (Justin and Jankowiak 2011). Ultra-high temperature ceramics (UHTC) are an emerging class of highly refractory structural materials capable of withstanding extreme environments (Johnson *et al.* 2009; Paul *et al.* 2012). They are borides and carbides of the early transition metals with high melting points ( $> 3000$  °C). The ability to form refractory oxide layers gives these materials the capability to withstand temperatures of  $2000$  °C or above (Gash *et al.* 2005; Levine *et al.* 2002). These compounds have strong covalent bonds and exhibit higher electrical and thermal conductivities than oxide ceramics. Diboride-based UHTCs have higher thermal conductivities than carbides and nitrides, which gives them good thermal shock resistance and makes them ideal for many high temperature thermal applications (Fahrenholtz *et al.* 2007).

Among the family of UHTCs materials, zirconium diboride ( $ZrB_2$ ) has exclusive combination of high mechanical properties, thermal and electrical conductivity, wear resistance, good oxidation and reasonable chemical attack resistances, and relatively low theoretical density ( $6.09$  g·cm<sup>-3</sup>). These properties have called attention to apply  $ZrB_2$  in aerospace systems that require exposure to extreme thermal and chemical environments, such as leading edges of hypersonic vehicles, rocket propulsion and for reusable atmospheric re-entry vehicles (Monteverde *et al.* 2008). Other non-aerospace applications include furnace heating elements, refractory crucibles for molten metal contact and plasma-arc electrodes, as well as cutting tools components and wear resistant devices (Neuman *et al.* 2013).

Despite their attractive properties and potential applications, processing costs and densification remain challenges for the fabrication of  $ZrB_2$ -based UHTC components (Guo 2009). Because of strong covalent bonding, low volume and grain boundary self-diffusion coefficients and the presence of surface oxide impurities, sintering of  $ZrB_2$ -based compositions is difficult (Sonber and Suri 2011). In most cases, dense  $ZrB_2$  ceramics without additives are obtained by hot pressing (HP) at  $2100$ – $2300$  °C, which is limited to simple geometric shapes. In addition to cost, fabrication of complex components requires expensive and time-consuming diamond machining to produce the desired shape from the pressed billet. Pressureless sintering offers a number of advantages over pressed-assisted processes, such as enabling the fabrication of components to near-net shape using standard powder-processing methods, and the production of multiple articles in a single furnace run (Chanberlain *et al.* 2006). Above all, the cost, time and material waste associated with diamond machining of the sintered parts can be substantially reduced.

Pressureless sintering (PLS), however, requires that the driving force for densification be a result of surface interactions among contacting particles. Because of this, it is rather difficult to densify pure  $ZrB_2$  ceramics by pressureless sintering without any additives due to its strong covalent bonding and low volume self-diffusion coefficients (Guo 2009). Various additives have been tried to improve the densification of  $ZrB_2$ . Metals, carbon, carbides, diborides and silicides were used to enhance the  $ZrB_2$  densification (Davi *et al.* 2016; Fahrenholtz *et al.* 2008; Sciti *et al.* 2006). A number of studies have shown that the introduction of SiC has beneficial effects not only to improve densification, but also on mechanical properties and oxidation resistance (Juliani *et al.* 2015; Zou *et al.* 2013; Zhang *et al.* 2008; Rezaie *et al.* 2007).

Starting particle size also affects  $ZrB_2$  densification behavior. Reducing  $ZrB_2$  particle size has been proved to enhance densification at lower sintering temperatures (Thompson *et al.* 2011; Fahrenholtz *et al.* 2008). However, the addition of sintering aids it is necessary to remove the oxygen content on the  $ZrB_2$  particle surface, which increases during the milling process to reduce particle size. Surface oxide impurities promote evaporation-condensation mechanisms, which led to the possibility of coarsening at temperatures below densification of  $ZrB_2$ . Small amounts of  $B_4C$  and C are the most studied additives to be used in sintering  $ZrB_2$  in order to react with the oxide impurities.

So far, the effect of particle size on  $ZrB_2$  densification was analyzed only for monolithic  $ZrB_2$ . This paper proposes to evaluate the effect of  $ZrB_2$  starting particle size on the pressureless sintering of  $ZrB_2/\beta$ -SiC composites containing different  $\beta$ -SiC volume fraction. The sintering behavior of the as-received relatively coarse  $ZrB_2$  powder (average diameter:  $14.2$   $\mu$ m) and the powder after planetary milling (average diameter:  $2.6$   $\mu$ m) was investigated in composites with  $\beta$ -SiC addition. The relative density, mechanical properties, microstructure and oxidation resistance were analyzed for two groups of composite with as-received and after-planetary milled  $ZrB_2$  matrix.

## EXPERIMENTAL

### MATERIALS

The used raw materials were ZrB<sub>2</sub> powder obtained from the ESK (Elektroschmelzwerk Kempten-Germany) and fine β-SiC powder, BF-12 grade (H.C. Starck-Germany). This ZrB<sub>2</sub> powder is mainly applied to refractory industry, and according to the supplier it presents Zr + B > 95 wt% and Carbon < 1.5 wt%. ZrB<sub>2</sub> powder was used both as-received (AZ) and after-planetary milling (MZ). Among high-energy ball mills, the planetary is a mechanically simple and versatile device for efficient grinding. It is usually made of two or more jars, rotating at an angular velocity  $\omega$  around their axis. ZrB<sub>2</sub> powder was milled using a polyethylene container in isopropanol with  $\alpha$ -SiC spheres (6 mm of diameter) during 6 h. Three different ball to powder ratio (BPR) were analyzed: 5:1, 7:1 and 10:1. The resulting SiC media contamination was determined by weighing the SiC balls before and after each milling condition. Particle size distributions of the as received and milled powder were measured by laser light scattering (Malvern Panalytical: Mastersizer 3000E). Morphology and powder size of ZrB<sub>2</sub> before and after milling were observed by Scanning electron microscopy (SEM – Model LEO 435i-Zeiss). The oxygen contents of the starting powders were measured by the LECO furnace method (Model TC500).

### METHODOLOGY

Four compositions were prepared with addition of 0, 10, 20 and 30 vol% of β-SiC to either as-received (AZ) or planetary-milled (MZ) ZrB<sub>2</sub> powder. The powder mixtures were ball milled for 4 h in isopropanol using SiC media. Subsequently, the slurries were dried by allowing the solvent to evaporate with a constant stirring to avoid particle sedimentation. The dried powder cakes were ground by pulverizing with an agate mortar and pestle and then sieved (-65 Mesh) to produce uniform granules for dry pressing. For the densification studies, 20 mm diameter and ~5 mm tall pellets were prepared by uniaxial dry pressing (DP) at 60 MPa followed by cold isostatic pressing (CIP) under 300 MPa. Pressureless sintering (PLS) was carried out in a graphite furnace in flowing argon atmosphere. Pressed samples were placed inside a graphite crucible and heated at 20–30 °C/min to 2050 °C for 1 h dwell time.

The bulk densities were measured by Archimedes' method with water as the immersing medium. The relative density was estimated by dividing the measured bulk density by a theoretical density (TD) value calculated using the mixture rule. Densities of 6.09 g·cm<sup>-3</sup> for ZrB<sub>2</sub> and 3.21 g·cm<sup>-3</sup> for SiC were used for the theoretical densities calculation. Microstructures were characterized using a scanning electron microscopy (SEM – Model LEO 435i-Zeiss) to observe the fracture surface of the sintered samples. X-ray diffraction (XRD- X'Pert Pro MPD Panalytical) was carried out to identify crystalline phases using a monochromated CuK $\alpha$ . Vickers microhardness (Future-Tech, model FM-7) was measured on polished surfaces with an applied load of 4.9 N and a dwell time of 15 s. At least ten indentations were made for each sample. Flexural strength at room temperature was measured on chamfered and polished bars of 35 mm × 4.0 mm × 3.5 mm (length × width × thickness, respectively). Four-point bending mode was used in a universal testing machine (Instron, model 4301) to measure the flexural strength over a 27/9 mm span at a crosshead speed of 0.5 mm/min using. The reported results are the average of at least 10 specimens.

Oxidation tests were carried out in polished bars of 2.0 × 2.5 × 15.0 mm. Sample weights (to an accuracy of 0.1 mg) and dimensions (to an accuracy of 0.001 cm) before oxidation were recorded and used to estimate mass change per unit area after oxidation. Samples were ultrasonically cleaned in isopropyl alcohol prior to exposure and were placed on an alumina crucible by resting them on the edge of the crucible to minimize the contact area. The tests were performed in a box furnace in stagnant air from room temperature (25 °C) to the desired temperature and time (1100 °C/4h and 1400 °C/1h). After that, the furnace with the samples inside was cooled to room temperature. XRD was used to identify the crystalline phases formed during oxidation process. SEM characterization was performed on the sample surfaces after oxidation exposure.

## RESULTS AND DISCUSSION

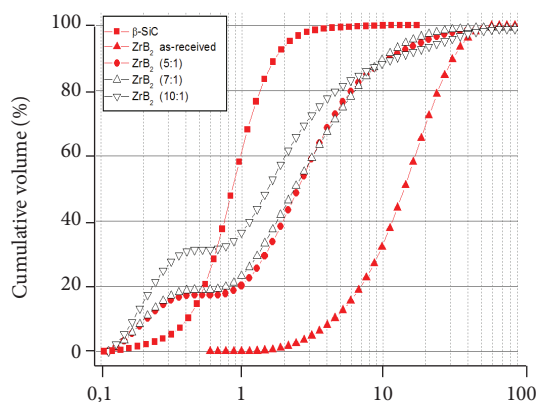
High Energy planetary milling of  $ZrB_2$  powder was very efficient in reducing particle size. The planetary ball mill is one of the most popular and most effective comminution processes. The average particle sizes of the planetary milled  $ZrB_2$  at different BPR are shown in Table 1. As-received  $ZrB_2$  had an initial average particle size of 14.2  $\mu m$ , which decreased to 1.5  $\mu m$  after milling with 10:1 BPR. The BPR has been established as an important parameter in ball milling that must be appropriately selected. In general, the higher the ball to powder weight ratio, the more effective the milling process is. This increased effectiveness is because the number of collisions per unit time increases with the number of balls. However, BPR of 10:1 resulted in  $ZrB_2$  powder with higher oxygen content and SiC milling media contamination of 3.8 wt% (Table 1). Considering these milled powder features, the milled  $ZrB_2$  with BPR of 5:1 was chosen to prepare the composites with  $\beta$ -SiC powder. This powder presented 2.0 wt% of SiC contamination, which is equivalent to 3.7 vol%. This  $\alpha$ -SiC content was considered to calculate the composite theoretical density and the total  $\alpha$ -SiC content after sintering (Table 2).

**Table 1.** Results of average size, SiC contamination and oxygen content of the as-received  $ZrB_2$  powder and after planetary milling with different BPR.

Powder features	$ZrB_2$ as received	$ZrB_2$ planetary milling (BPR *)		
		(5:1)	(7:1)	(10:1)
Average size ( $\mu m$ )	14.2	2.6	2.3	1.5
SiC wt% contamination	–	2.0	2.8	3.8
Oxygen content	$0.40 \pm 0.04$	$1.22 \pm 0.06$	$1.69 \pm 0.04$	$2.56 \pm 0.03$

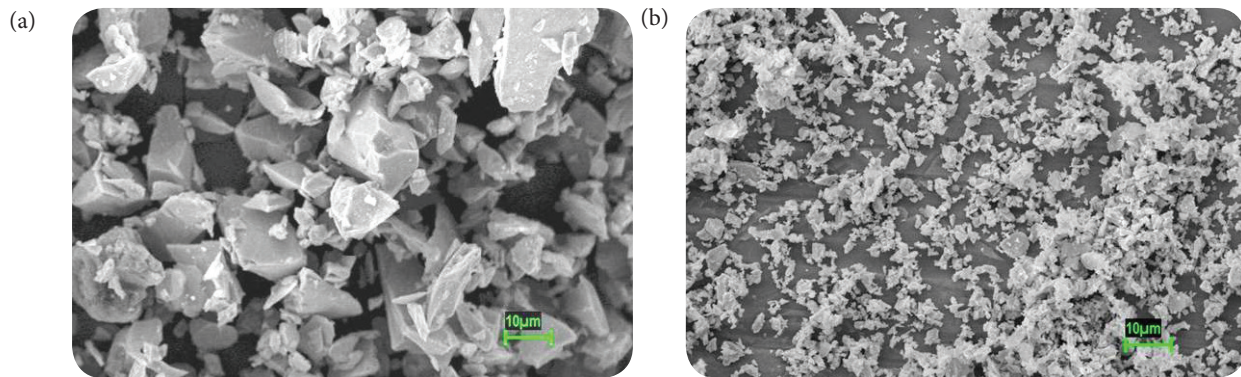
\*BPR-ball to powder ratio.

Figure 1 shows the particle size distribution of  $\beta$ -SiC and as-received and milled  $ZrB_2$  powders. Powders used to prepare the composites are in red color. It can be seen the significant reduction of  $ZrB_2$  particle size distribution after planetary milling. The curves of the milled  $ZrB_2$  show a bimodal distribution of particle size. There is a coarser distribution between around 80 to 0.5  $\mu m$ , and a finer distribution around 0.5 to 0.1  $\mu m$ . SiC powder is relatively finer with an average particle size of 0.8  $\mu m$ .



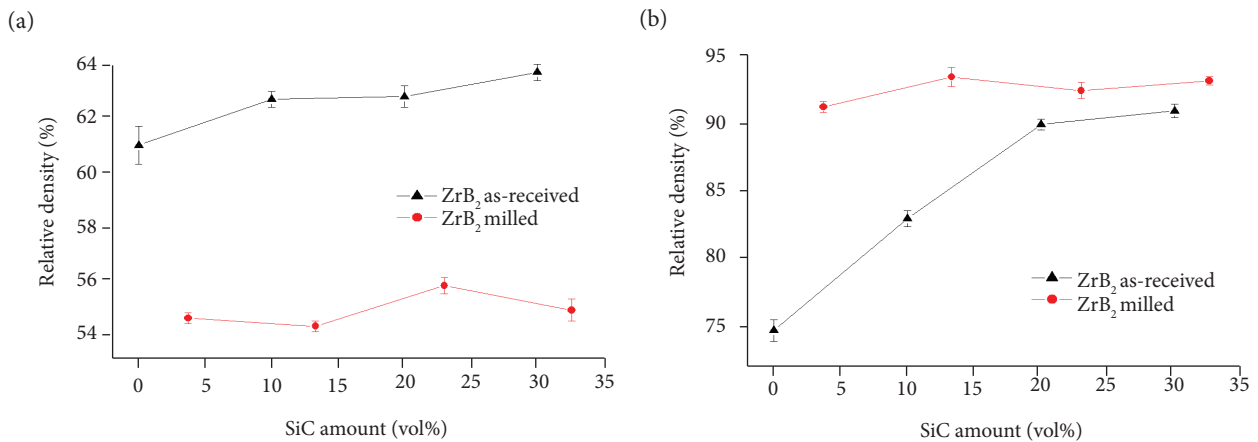
**Figure 1.** Particle size distribution of SiC as-received and milled  $ZrB_2$  powders with different BPR. The used powders to prepare the composites are in red color.

Figure 2 shows SEM micrographs of as-received  $ZrB_2$  powder and after-planetary milling with 5:1 BPR. The particle sizes and morphology of the powders are in accordance with the particle size distribution (Fig. 1), showing significant particle size reduction after planetary milling.



**Figure 2.** SEM micrograph of  $ZrB_2$  powder: (a) as-received and (b) after-planetary milling with 5:1 BPR.

Figure 3 shows the relative density results of  $ZrB_2$ -SiC samples after CIP (Fig. 3a) and after PLS (Fig. 3b) as a function of SiC content. Table 2 shows the values of SiC vol% fraction and theoretical densities calculated from the rule of mixtures used to obtain the relative densities plotted in Fig. 3. The SiC media contamination was taken into account to calculate the theoretical density of MZ-SiC composites.



**Figure 3.** Relative density of  $ZrB_2$ -SiC composites as a function of SiC content: (a) after CIP compaction; (b) after PLS at 2050 °C/1h.

**Table 2.** SiC vol% and theoretical densities of the prepared composites.

AZ-SiC		MZ-SiC	
SiC vol%	Theoretical density [ $g \cdot cm^{-3}$ ]	SiC vol%	Theoretical density $g \cdot cm^{-3}$
0	6.09	3.7	5.984
10	5.802	13.3	5.707
20	5.514	22.9	5.429
30	5.226	32.6	5.152

Figure 3a shows the difference of green densities between composites prepared with distinct initial  $ZrB_2$  particle sizes. Pressed composites with coarser  $ZrB_2$  initial particle size show higher green densities than composites with milled  $ZrB_2$  powder. The coarser particle size distribution leads to a better powder packing, resulting in higher green density. For AZ composites, the increase in SiC content leads to a slight increase in green density. Figure 4 shows the fracture surface microstructure of the CIP samples AZ-10SiC and MZ-10SiC. It can be seen the difference in particle sizes between two samples that give rises to green densities difference.

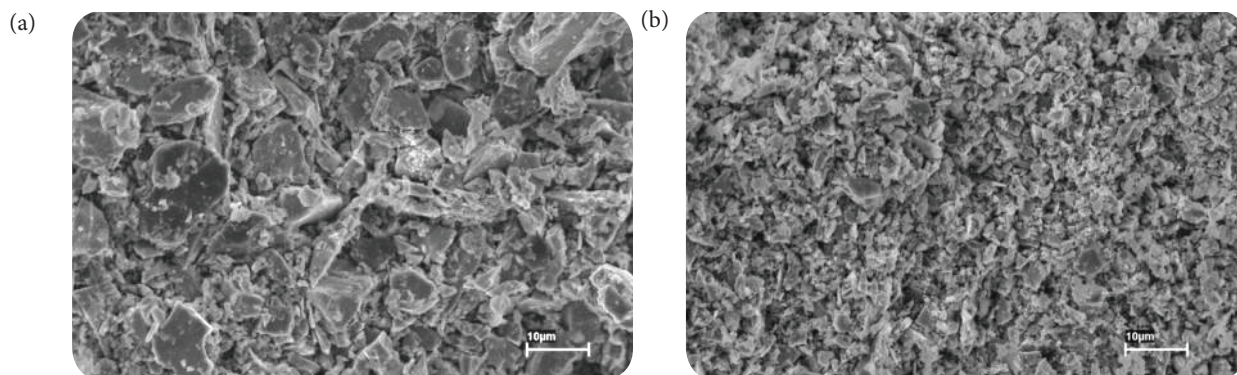


**Figure 4.** SEM micrographs of the fracture surface of samples after CIP compaction: (a) AZ-10SiC and (b) MZ-10SiC.

Although the higher initial green densities, samples with coarser  $ZrB_2$  showed lower final densification after sintering (Fig. 3b). AZ without SiC addition exhibited the lowest relative density ( $74.7 \pm 0.7$  %TD). As SiC concentration increased in samples AZ, the relative density increased reaching values of  $90.8 \pm 0.7$  for composite AZ-30SiC. Composites prepared with MZ showed higher densification regardless of the SiC concentration. Theoretical densities were between 91 and 93 %TD. These results suggest that densification of  $ZrB_2$  and  $ZrB_2$ -SiC composites are greatly facilitated by the powder size reduction even though the higher oxygen content. Reducing the starting particle size appeared to increase the driving force for densification by the increasing in surface area.

X-ray diffraction patterns of  $ZrB_2$ -SiC sintered at  $2050$  °C/1h (Fig. 5) showed the presence of two main phases, i.e.,  $ZrB_2$  and  $\alpha$ -SiC polytypes in both set of composites prepared with AZ and MZ powders. No other phase (oxides or compounds with Zr and Si) is found in any sintered composite, showing no formation of solid solution between  $ZrB_2$  and SiC. The initial cubic  $\beta$ -SiC (3C) powder was transformed in a mixture of hexagonal  $\alpha$ -SiC during sintering at high temperature. The 4H and 6H polytypes of  $\alpha$ -SiC were the predominate polytypes. Due to the significant overlap of the Bragg reflections from the different SiC polytypes, it is not possible to verify the co-existence of  $\beta$  (3C) and  $\alpha$  (4H and 6H) SiC polytypes.

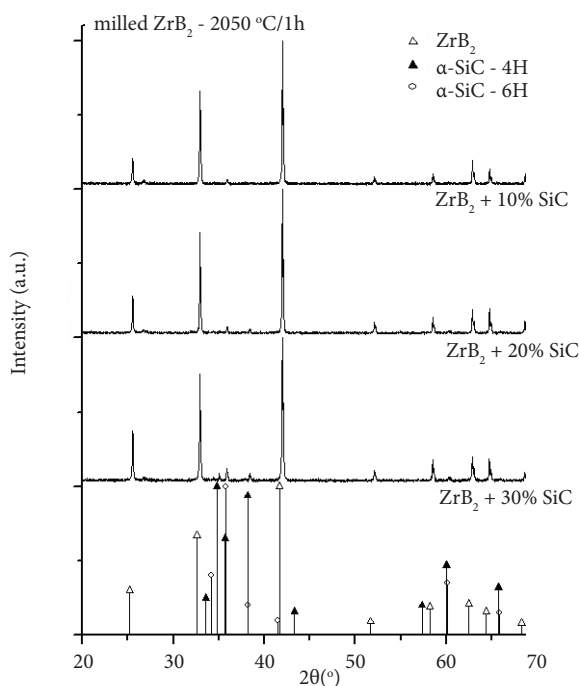
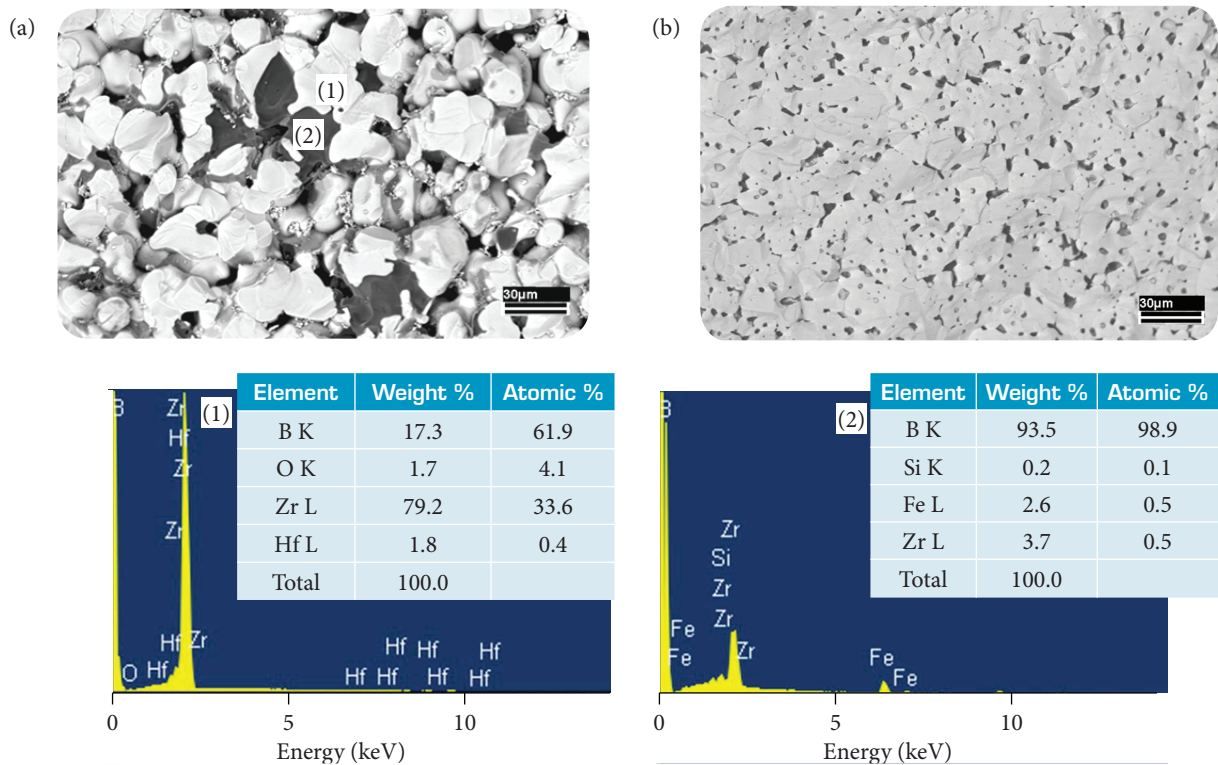


**Figure 5.** XRD patterns of the MZ-SiC composites after sintering at  $2050$  °C/1h.

Figure 6 shows SEM images of the fracture surface of the ZrB<sub>2</sub> without β-SiC addition and the energy dispersive spectroscopy (EDS) spectrum of two different regions of AZ sample. The microstructure of two samples is very different with the AZ sample showing large grains and high porosity while MZ shows smaller grain size and pore fraction compared to that of AZ microstructure. Using back scattered electron (BSE) image, a dark grey phase was observed throughout the AZ microstructure. EDS analysis shows that this phase is predominantly composed by boron (Fig. 6a, region 2). The presence of this boron-containing phase is related to the ZrB<sub>2</sub> synthesis process. According to the powder supplier, this ZrB<sub>2</sub> powder is manufactured by a boro-carbothermal process from the raw materials boron oxide, zirconium oxide and carbon in an arc furnace at temperatures above 2400 °C. Concurrently, the following reaction (Eq. 1) takes place:



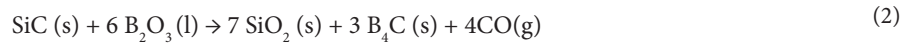
The resultant gray-silver crystals are separated from unreacted material, ground and classified in further preparation steps. Depending on its further use, the material is ground until in the micron range. The EDS of region 1 indicates the elements of light grey phase, which corresponds to ZrB<sub>2</sub> grains.



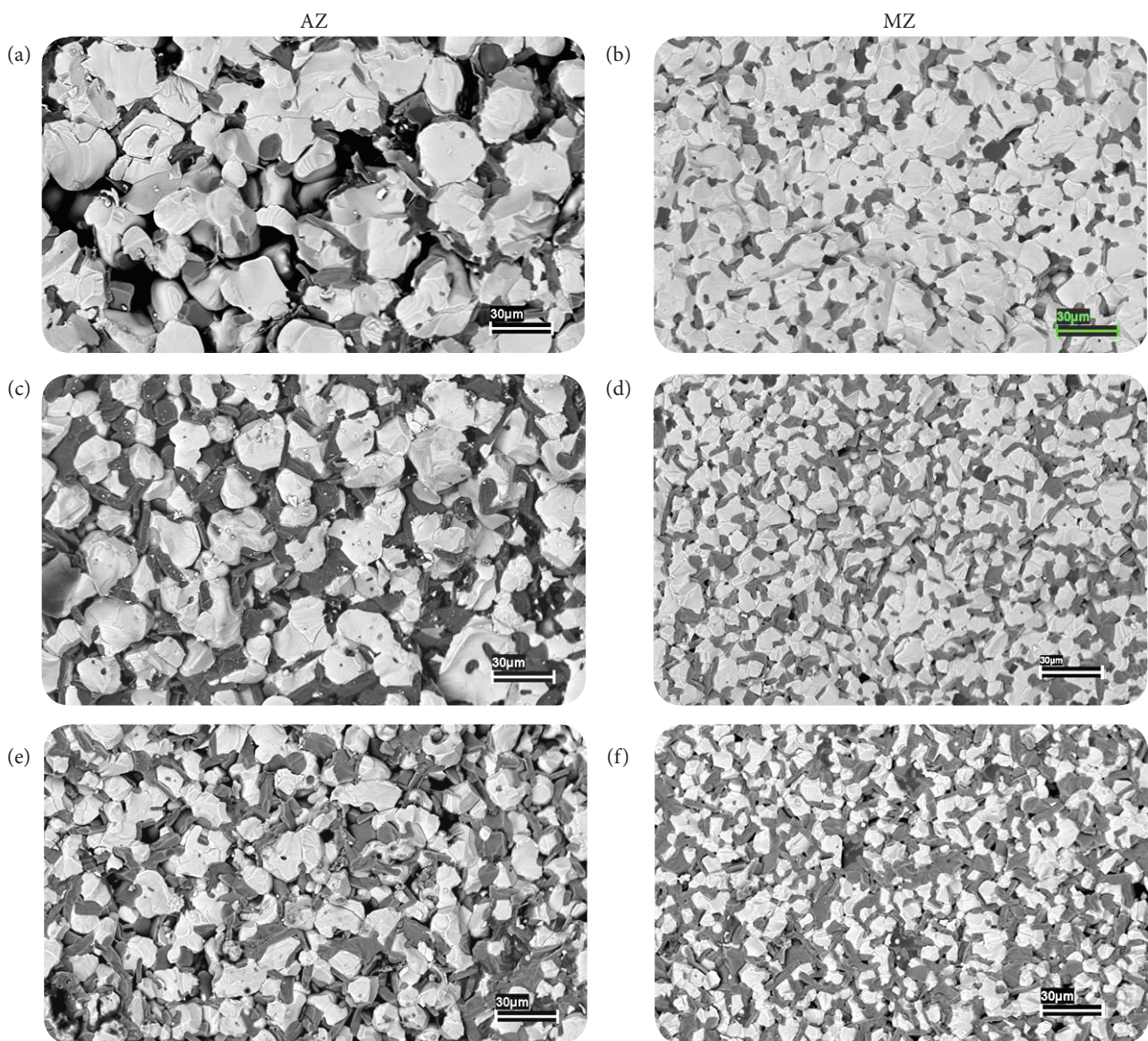
**Figure 6.** SEM images of sintered ZrB<sub>2</sub> without SiC addition, and EDS of two different phases of sample AZ [region 1 and 2]: (a) AZ; (b) MZ.

Figure 7 shows SEM images of the fracture surface of the PLS ZrB<sub>2</sub>-SiC composites. Two majority phases can be clearly distinguished in backscattered electron (BSE) images. BSE image analysis confirms that light gray phase is ZrB<sub>2</sub> grains and dark gray phase is SiC grains. Sintering with MZ powder promoted a finer microstructure with smaller ZrB<sub>2</sub> grain size and SiC grains uniformly dispersed in the ZrB<sub>2</sub> matrix (Figs. 7b, 7d and 7f) compared with AZ composites (Figs. 7a, 7c and 7e). Equiaxed ZrB<sub>2</sub> grains with an average size range from 30 to 18 μm and 16 to 9 μm were observed in composites with AZ and MZ, respectively. Micrograph of composites with MZ presents virtually pore-free microstructure (Figs. 7b, 7d and 7f).

All micrographs show fracture surfaces with a transgranular aspect and a significant reduction of  $ZrB_2$  grain size with increasing SiC content. The growth of the  $ZrB_2$  matrix grains is probably inhibited by SiC particles by pinning of the  $ZrB_2$  grain boundaries during sintering. Moreover, the grain growth is also restricting by the removal of intergranular oxide impurities as  $B_2O_3$  with reaction with SiC, as shown in the following reaction (Eq. 2) (Zhang *et al.* 2008).



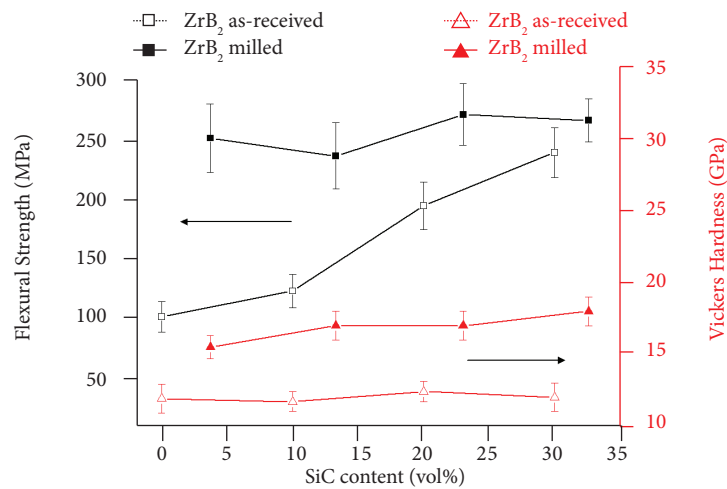
The morphology of  $ZrB_2$  grains is equiaxed, while SiC grains appear to be elongated (Fig. 7). The platelet SiC grain morphology is result of the very fine SiC particle size starting powder and can be explained using the percolation theory (Zhang *et al.* 2008). Besides,  $\alpha$ -SiC phase transformation with the associated platelet like grains morphology can also improve mechanical properties such as fracture toughness.



**Figure 7.** SEM (BSE) images depicting the microstructures of the  $ZrB_2$ -SiC composites processed with AZ and MZ powder sintered at 2050/1h: (a) and (b) 10% SiC; (c) and (d) 20% SiC; (e) and (f) 30% SiC.

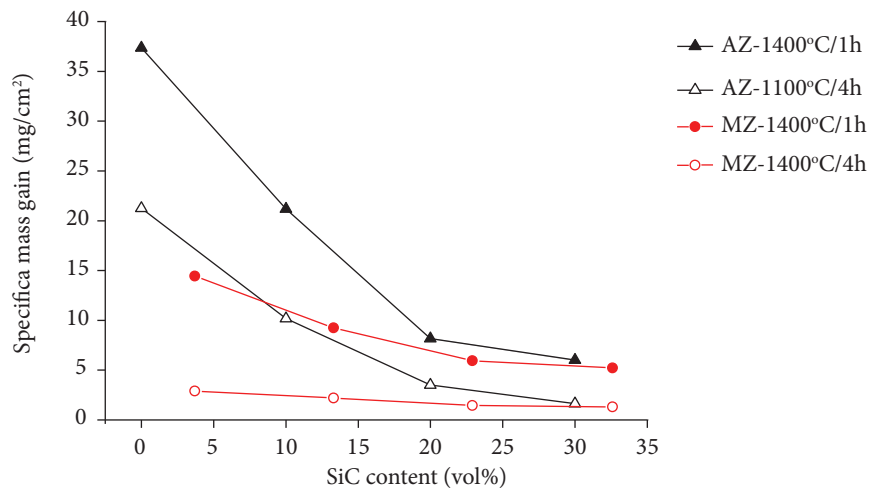


Figure 8 shows the correlation between mechanical properties as flexural strength and micro hardness with SiC content. Samples with MZ show the highest flexural strength regardless SiC content with average results of 260 MPa for all compositions, including for ZrB<sub>2</sub> without β-SiC addition. Composites prepared with MZ had higher strengths as a result of smaller grains and higher densification. On the other hand, flexural strength of composites with AZ was smaller than sintered with MZ, varying from 112 ± 13 for pure ZrB<sub>2</sub> to 241 ± 21 MPa for sample AZ-30SiC. The relative higher grain size and higher porosity of samples processed with AZ may be responsible for the lower flexural strength. Besides that, as SiC increased in samples with AZ, the flexural strength increased because of the reduction of porosity and the ZrB<sub>2</sub> matrix grain size. Micro hardness of the composites varied significantly with initial ZrB<sub>2</sub> particle size. For samples prepared with AZ, the average micro hardness value was around 12.5 GPa, regardless of SiC amount. For samples prepared with MZ, the average micro hardness was 17.5 GPa.



**Figure 8.** Flexural strength and micro hardness as a function of SiC content of ZrB<sub>2</sub>-SiC composites processed with AZ and MZ powder sintered at 2050 °C/1h.

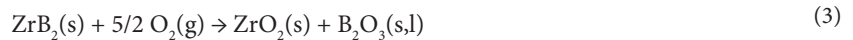
Figure 9 shows the oxidation resistance through specific mass gain as a function of SiC content. Samples processed with AZ and MZ were oxidized in two long-term thermal treatment in stagnant air: 1100 °C/4h and 1400 °C/1h. The starting size of the



**Figure 9.** Specific mass gain of ZrB<sub>2</sub>-SiC composites as function of SiC content after oxidation at 1100 °C/4h and at 1400 °C/1h. Composites processed with different ZrB<sub>2</sub> particle size.

ZrB<sub>2</sub> powder modified the composites oxidation behavior. Samples sintered with MZ presented lower oxidation than sintered with AZ for both thermal oxidation treatments. However, the difference in mass gain between samples with different starting particle size decreased as the SiC content increased. For samples prepared with AZ, the mass gain at 1400 °C/1h decreased from 37.4 to 6.0 mg/cm<sup>2</sup> as SiC concentration increased from 0 to 30 vol%. While for specimens prepared from MZ, the mass gain at 1400 °C/1h decreased from 14.4 mg/cm<sup>2</sup>, which is less than a half of the value determined to AZ composite, to 5.3 mg/cm<sup>2</sup> as SiC concentration increased from 3.7 to 32.6 vol%. The same effect was observed for samples oxidized at 1100 °C/4h. This effect could be explained by the porosity and the larger ZrB<sub>2</sub> grain size of samples sintered with AZ powder.

The increase in SiC content decreased de ZrB<sub>2</sub>-SiC composite oxidation for both thermal cycles, although oxidation was more severe at 1400 °C/1h than at 1100 °C/4h. These results can be explained by the ZrB<sub>2</sub> and SiC oxidation behavior and mechanisms. Below 1200 °C, ZrB<sub>2</sub>-SiC composites behave like pure ZrB<sub>2</sub>, since they undergo oxidation more quickly than SiC, thus giving a passive B<sub>2</sub>O<sub>3</sub> glassy surface layer and forming a porous ZrO<sub>2</sub> crystalline solid (Eq. 3). This effect could be observed in samples prepared with MZ oxidized at 1100 °C/4h, which showed little difference in oxidation with the increasing in SiC content. MZ composite had mass gain of 2.9 mg/cm<sup>2</sup> for 3.7 vol% SiC and 1.3 mg/cm<sup>2</sup> for sample with 32.6 vol% SiC (Fig. 9). On the other hand, composites with AZ oxidized at 1100 °C showed a more pronounced decrease in mass gain with the increase in SiC content varying from 21.5 mg/cm<sup>2</sup> for pure AZ to 1.6 mg/cm<sup>2</sup> for AZ-30SiC. The high porosity of AZ samples exposes a higher specific surface area to react with the oxygen, increasing this way the amount of mass gain. As SiC increased, the AZ samples porosity decreased and consequently the mass gain decreased:



As temperature increases, the liquid B<sub>2</sub>O<sub>3</sub> layer evaporates leaving an exposed porous ZrO<sub>2</sub>, which does not protect the underlying ZrB<sub>2</sub> from oxidation (Fahrenholtz and Hilmas 2012). The addition of SiC improves the oxidation resistance of ZrB<sub>2</sub> at 1100 °C and above by the formation of a borosilicate glass closing the pores and covering the exposed surface, according to the following reaction (Eq. 4):



The silica-rich layer formed is refractory and then provides resistance to oxygen diffusion, protecting the composite from further oxidation effectively up to at least ~1500 °C.

XRD was used to detect the phases of the oxidation products on the sample surface. Figure 10 shows the diffraction pattern of the sample MZ-30SiC oxidized at 1100 °C/4h and at 1400 °C/1h. The major peaks in both XRD patterns can be indexed to monoclinic ZrO<sub>2</sub> (powder diffraction file (PDF) card number 01-080-0966). ZrO<sub>2</sub> peaks intensity is significantly higher in sample oxidized at 1100 °C/4h. B<sub>2</sub>O<sub>3</sub> crystalline phase is identified in sample oxidized at 1100 °C/4h, while sample oxidized at 1400 °C/1h shows an amorphous halo, probably formed from the borosilicate glassy phase. XRD of oxidized AZ-10SiC and AZ-20SiC showed similar diffractogram patterns of AZ-30SiC for both heat treatments.

Figure 11 shows SEM backscattered electron images of the polished surface of AZ-30SiC composites oxidized in stagnant air atmosphere at 1100 °C/4h (Fig. 11a) and at 1400 °C/1h (Fig. 11b). Small ZrO<sub>2</sub> crystals are observed on the ZrB<sub>2</sub> grains after oxidation at 1100 °C/4h. Oxidation at 1400 °C/1h leads to dendritic crystals growth of ZrO<sub>2</sub>, which are partially embedded in the borosilicate glass. The SEM observations are in accordance with the XRD results, where ZrO<sub>2</sub> and B<sub>2</sub>O<sub>3</sub> were identified in sample oxidized at 1100 °C, while smaller intensity peaks of ZrO<sub>2</sub> and a glassy phase were identified in sample oxidized at 1400 °C. SEM images of the oxidized MZ-30SiC showed the same microstructure observed for AZ-30SiC composites.

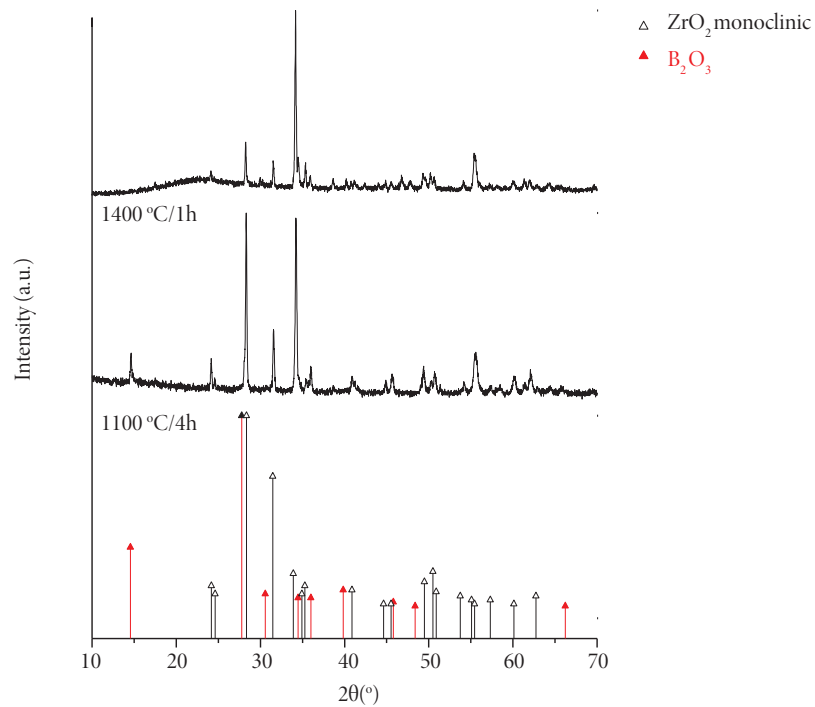


**Figure 10.** XRD patterns of MZ-30SiC composite oxidized at 1100 °C/4h and 1400 °C/1h.

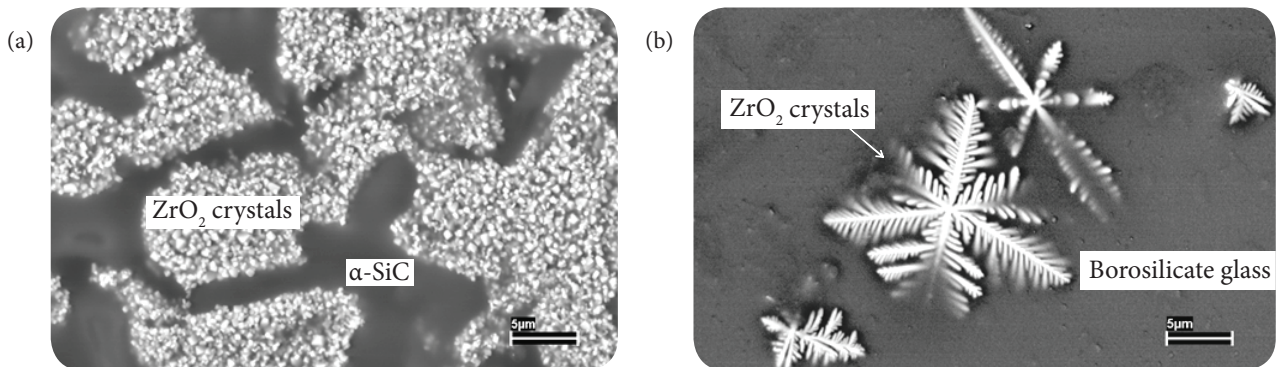


**Figure 11.** SEM images of the surface of AZ-30SiC composite after oxidation: (a) 1100 °C/4h; (b) 1400 °C/1h.

## CONCLUSION

Ultra high temperature ceramics of  $ZrB_2$ -SiC composites were produced by pressureless sintering using  $ZrB_2$  powders with two different particle size distributions, as-received (AZ) and after-planetary milling (MZ). The high-energy milling promoted a significant reduction of  $ZrB_2$  particle powder, from 14.2  $\mu\text{m}$  for as-received to 2.6  $\mu\text{m}$  after-planetary milling with 5:1 BPR. This powder presented 1.22 wt% of oxygen compared to 0.4 wt% of the AZ powder and 2.0 wt% of SiC media contamination. However, the reduction of  $ZrB_2$  particle size led to better results of densification, mechanical properties and oxidation resistance of the MZ-SiC composites compared to AZ-SiC composites. Increasing SiC content in the composites promoted a reduction in  $ZrB_2$  grain size for both set of composites. The SiC addition to the MZ powder did not promote significant improvement in relative density and mechanical properties with relative density of  $91.1 \pm 0.4$  and  $93.0 \pm 0.5$  %TD, for lower and higher SiC content, respectively.

Composites prepared with MZ showed the highest flexural strength ( $268 \pm 18$  MPa) and micro hardness ( $18 \pm 1$  GPa). On the other hand, composites with AZ powder presented an increasing in relative density and flexural strength with increasing in SiC addition. X-ray diffraction analysis of ZrB<sub>2</sub>-SiC composites identified, besides ZrB<sub>2</sub> crystalline phase, the corresponding phases of the 4H and 6H  $\alpha$ -SiC polytypes. The increase in SiC content decreased the ZrB<sub>2</sub>-SiC composite oxidation for both thermal cycles, although oxidation was more severe at 1400 °C/1h than at 1100 °C/4h. Small ZrO<sub>2</sub> crystals were observed on the ZrB<sub>2</sub> grains after oxidation at 1100 °C/4h, and dendritic crystals growth of ZrO<sub>2</sub> partially embedded in the borosilicate glass were observed on sample oxidized at 1400 °C/1h. These findings could also be confirmed from the XRD analysis of the oxidized surface.

---

## AUTHOR'S CONTRIBUTION

Conceptualization, Rocha RM; Methodology, Rocha RM; Investigation, Rocha RM, Juliani JO, Davi CO, Sene FF; Writing – Original Draft, Rocha RM, Juliani JO, Davi CO; Writing – Review and Editing, Rocha RM; Funding Acquisition, Rocha RM.

---

## ACKNOWLEDGMENTS

The authors gratefully acknowledge to Dr. Sérgio Luis G. Petroni from IAE due to LECO oxygen analysis.

---

## FUNDING

Conselho Nacional de Desenvolvimento Científico e Tecnológico [<https://doi.org/10.13039/501100003593>]  
Grant no. 402171/2013-6

---

## REFERENCES

- Boyd ID, Padilla JF (2003) Simulation of sharp leading edges aerothermodynamics. Presented at: 12th AIAA International Space Planes and Hypersonic Systems and Technologies Conference; Norfolk, USA. <https://doi.org/10.2514/6.2003-7062>
- Chamberlain AL, Fahrenholtz WG, Hilmas GE (2006) Pressureless sintering of zirconium diboride. *J Am Ceram Soc* 89(2):450-456. <https://doi.org/10.1111/j.1551-2916.2005.00739.x>
- Davi CO, Yassuda MKH, Rocha RM (2016) Effect of TiB<sub>2</sub> on Pressureless sintering and hot pressing of ZrB<sub>2</sub>. *Mater Sci For* 881:97-102. <https://doi.org/10.4028/www.scientific.net/MSF.881.97>
- Fahrenholtz WG, Hilmas GE, Talmy IG, Zaykoski JA (2007) Refractory diborides of zirconium and hafnium. *J Am Ceram Soc* 90(5):1347-1364. <https://doi.org/10.1111/j.1551-2916.2007.01583.x>
- Fahrenholtz WG, Hilmas GE, Zhang SC, Zhu S (2008) Pressureless sintering of zirconium diboride: particle size and additive effects. *J Am Ceram Soc* 91(5):1398-13404. <https://doi.org/10.1111/j.1551-2916.2007.02169.x>
- Fahrenholtz WG, Hilmas GE (2012) Oxidation of ultra-high temperature transition metal diboride ceramics. *Inter Mater Rev* 57(1):61-72. <https://doi.org/10.1179/1743280411Y.0000000012>
- Gasch MJ, Elerby DT, Johnson SM (2005) Ultra high temperature ceramic composites. In: Bansal NP, editor. *Handbook of Ceramic Composites* (p.197-224). New York: Springer. [https://doi.org/10.1007/0-387-23986-3\\_9](https://doi.org/10.1007/0-387-23986-3_9)
- Guo SG (2009) Densification of ZrB<sub>2</sub>-based composites and their mechanical and physical properties: A review. *J Eur Ceram Soc* 29(6):995-1011. <https://doi.org/10.1016/j.jeurceramsoc.2008.11.008>
- Johnson SM, Gasch M, Stackpoole M, Lawson JW, Gusman M (2009) Recent developments in ultra high temperature ceramics at NASA ames. Presented at: 16th AIAA/DLR/DGLR International Space Planes and Hypersonic Systems and Technologies Conference; Bremen,

Germany. <https://doi.org/10.2514/6.2009-7219>

Juliani MO, Davi CO, Rocha RM (2015) Pressureless sintering of ZrB<sub>2</sub> with β-SiC addition. Mater Sci For 820:250-255. <https://doi.org/10.4028/www.scientific.net/MSF.820.250>

Justin JF, Jankowiak A (2011) Ultra High Temperature Ceramics - densification properties and thermal stability. J Aerospace Lab 3(8):1-11.

Kontinos DA, Gee K, Prabhu DK (2001) Temperature constraints at the sharp leading edge of a crew transfer vehicle. Presented at: 35th AIAA Thermophysics Conference; Ahahein, USA. <https://doi.org/10.2514/6.2001-2886>

Levine SR, Opila EJ, Halbig MC, Kiser JD, Singh M, Salem JA (2002) Evaluation of ultra-high temperature ceramics for aeropropulsion use. J Eur Ceram Soc 22(14-15):2757-2767. [https://doi.org/10.1016/S0955-2219\(02\)00140-1](https://doi.org/10.1016/S0955-2219(02)00140-1)

Loehman R, Corral E, Dumm HP, Kotula P, Tandon R (2006) Ultra-high temperature ceramics for hypersonic vehicle applications. (SAND 2006-2925). Sandia Report.

Monteverde F, Bellosi A, Scatteia L (2008) Processing and properties of ultra-high temperature ceramics for space applications. Mater Sci Eng A 485(1-2):415-421. <https://doi.org/10.1016/j.msea.2007.08.054>

Neuman EW, Hilmas GE, Fahrenholtz WG (2013) Strength of zirconium diboride to 2300 °C. J Am Ceram Soc 96(1):47-50. <https://doi.org/10.1111/jace.12114>

Opeka MM, Talmy IG, Zaykoski JA (2004) Oxidation-based materials selection for 2000°C + hypersonic aerosurfaces: theoretical considerations and historical experience. J Mater Sci 39(19):5887-5904. <https://doi.org/10.1023/B:JMSC.0000041686.21788.77>

Paul A, Jayaseelan DD, Venugopal S, Zapata-Solvas E, Binner J, Vaidhyanathan B, Heaton A, Brown P, Lee WE (2012) UHTC composites for hypersonic applications-Refractory non-oxides protect leading edges of hypersonic vehicles during flight. Am Ceram Soc Bull 91(1):22-29.

Rezaie A, Fahrenholtz WG, Hilmas GE (2007) Effect of hot pressing time and temperature on the microstructure and mechanical properties of ZrB<sub>2</sub>-SiC. J Mater Sci 42(8):2735-2744. <https://doi.org/10.1007/s10853-006-1274-2>

Rolim TC, Toro PGR, Minucci MAS, Oliveira AC, Follador RC (2011) Experimental results of a Mach 10 conical-flow derived waverider to 14-X hypersonic aerospace vehicle. J Aerosp Technol Manag 3(2):127-136. <https://doi.org/10.5028/jatm.2011.03027510>

Sciti D, Guicciardi S, Bellosi A, Pezzoti G. (2006) Properties of a pressureless-sintered ZrB<sub>2</sub>-MoSi<sub>2</sub> ceramic composite. J Am Ceram Soc 89(7):2320-2322. <https://doi.org/10.1111/j.1551-2916.2006.00999.x>

Sonber JK, Suri AK (2011) Synthesis and consolidation of zirconium diboride: review. Adv Appl Ceram 110(6):321-334. <https://doi.org/10.1179/1743676111Y.0000000008>

Squire TH, Marschall J (2010) Material property requirements for analysis and design of UHTC components in hypersonic applications. J Eur Ceram Soc 30(11):2239-2251. <https://doi.org/10.1016/j.jeurceramsoc.2010.01.026>

Sziroczak D, Smith H (2016) A review of design issues specific to hypersonic flight vehicles. Progress Aero Sci 84:1-28. <https://doi.org/10.1016/j.paerosci.2016.04.001>

Thompson M, Fahrenholtz WG, Hilmas GE (2011) Effect of starting particle size and oxygen content on densification of ZrB<sub>2</sub>. J Am Ceram Soc 94(2):429-435. <https://doi.org/10.1111/j.1551-2916.2010.04114.x>

Van Wie DM, Drewry DG, King DE, Hudson CM (2004) The hypersonic environment: required operating conditions and design challenges. J Mater Sci 39(19):5915-5924. <https://doi.org/10.1023/B:JMSC.0000041688.68135.8b>

Walker SP, Sullivan BJ (2003) Sharp refractory composites leading edges for hypersonic vehicles. Presented at: 12th AIAA International Space Planes and Hypersonic Systems and Technologies Conference; Norfolk, USA. <https://doi.org/10.2514/6.2003-6915>

Zhang SC, Hilmas GE, Fahrenholtz WG (2008) Pressureless sintering of ZrB<sub>2</sub>-SiC ceramics. J Am Ceram Soc 91(1):26-32. <https://doi.org/10.1111/j.1551-2916.2007.02006.x>

Zou J, Zhang GJ, Zhang H, Huang ZR, Vleugels J, Biest OV (2013) Improving high temperature properties of hot pressed ZrB<sub>2</sub>-20 vol% SiC ceramic using high purity powders. Ceram Inter 39(1):871-876. <https://doi.org/10.1016/j.ceramint.2012.06.018>